SAND2018-11638

SANDIA REPORT

SAND2002-xxxx
Unlimited Release
Printed September 2018

Measurement of the low-energy germanium quenching factor with a small-mass detector

Belkis Cabrera-Palmer

Prepared by
Sandia National Laboratories
Albuquerque, New Mexico 87185 and Livermore, California 94550

Sandia National Laboratories is a multimission laboratory managed and operated by National Technology and Engineering Solutions of Sandia, LLC, a wholly owned subsidiary of Honeywell International, Inc., for the U.S. Department of Energy's National Nuclear Security Administration under contract DE-NA0003525.

Sandia National Laboratories

Issued by Sandia National Laboratories, operated for the United States Department of Energy by National Technology and Engineering Solutions of Sandia, LLC.

SAND2002-xxxx
Unlimited Release
Printed September 2018

Measurement of the low-energy germanium quenching factor with a small-mass detector

Belkis Cabrera-Palmer
Rad/Nuc Detection Systems
Sandia National Laboratories
bcabrer@sandia.gov

Abstract

We report on work performed to measure the quenching factor of low kinetic energy germanium recoils, as a collaboration between Sandia National Laboratories (SNL) and Duke University. A small-mass low-noise high purity germanium detector was irradiated by a mono-energetic pulsed neutron beam produced by the Triangle Universities Nuclear Laboratory (TUNL) Van-de-Graaff accelerator. Data was collected to determine the germanium quenching factor as a function of 10 discrete recoil energy values in the range $\sim [0.8, 5.0]$ keVnr. We describe the experiment, present the simulation and data processing for the 10 datasets, and discussed the quenching factor analysis result for one of them. This one result seems to indicate a somewhat large deviation from literature values, though it is still preliminary to claim the presence of a systematic bias in our data or analysis.

Acknowledgment

We thank our Duke University collaborators Long Li, Sam Hedges, Connor Awe and Phil Barbeau for performing the measurements, and for their valuable inputs and feedback on the data analysis. We thank David Reyna for his support which enabled this work. We thank Erik Brubaker for the very useful discussions during the execution of this work.

Contents

List of Figures

List of Tables

Nomenclature

TUNL Triangle Universities Nuclear Laboratory

PSD Pulse Shape Discrimination

CEνNS Coherent Elastic Neutrino-Nucleus Scattering

ULEGe Ultra Low energy Germanium

TOF time-of-flight

FWHM Full Width at Half Maximum

RMS or rms Root Mean Square

Chapter 1

Introduction

Accurate knowledge of the quenching factor for low energy germanium nucleus recoils is of significant relevance to the basic science community, from cutting edge experiments in dark matter searches [3] to the neutrino physics community. In particular, germanium detectors constitute an ideal technology for the observation and cross-section characterization of the Coherent Elastic Neutrino-Nucleus Scattering (CEνNS) [5], for which the detection signal is, in most cases, the quenched ionization energy generated by nuclear recoils.

Furthermore, improvements in the understanding of the low-energy neutron recoils within germanium detectors could potentially expand the options and capabilities for emergency response to identify radiological threats. Since germanium detectors are standard equipment for emergency responders, the ability to gain simultaneous information on neutrons as well as gammas from a single system could prove useful. Current germanium systems are not optimized for low-noise response, but future systems could take advantage of the developments that have been made in the basic science community. For such a system, accurate knowledge of the low-energy responses for neutron recoils could directly translate to an ability to extract spectral information for fission-energy neutrons with a germanium detector.

Here, we report on work performed to measure the quenching factor of low kinetic energy germanium nuclei, as a collaboration between Sandia National Laboratories (SNL) and Duke University. Most of the experimental work was done at the Triangle Universities Nuclear Laboratory (TUNL), where a Van-de-Graaff accelerator can produce pulsed beams mono-energetic neutrons ideal for quenching factor measurements. For this measurement, SNL provided a 11.3 mm (diameter) x 5.3 mm (length) n-type point contact germanium detector, model Ultra-LEGe GUL0055, manufactured by Canberra Industries. Several features make this detector attractive for quenching factor measurements. First, due to its small germanium mass (only 3 g), the expected number of multiple neutron scatter in the germanium element is negligible, compared to large mass detectors used previously [6]. Multiple scatters events are not desired since they span several germanium recoil energies. Second, the manufacturer-reported very-low noise (114 eV FWHM at 5.9 keV) enable the detection of recoils producing low ionization energy depositions. An array of backing detectors to register the scattered neutrons was readily available at TUNL.

Two analysis pipelines have been independently developed by each institution. In this report, we present the simulation and analysis approach executed by SNL. At the time of this report, all the simulations and the data processing stage have been completed. However, the SNL final

analysis to derive the quenching factor has only been culminated for one of the measured recoil energy points, mainly due to the computational intensity of our chosen fitting procedure. Since the analysis procedure is already in place, results for the full set of measured recoil energies should follow soon. Comparison with the Duke results, once these become available, will validate the two analysis pipelines.

Chapter 2

Experimental setup

Measurements with the TUNL accelerator were performed during four scheduled periods: September 2017, October 2017, February 2018 and March 2018. The main components of the experimental setup were: the neutron beam, the germanium detector, and the backing detectors that register the scattered neutrons. Target reaction ^{7}Li(p,n) was chosen to generate nearly monochromatic neutron beams starting from 580 keV that allow the low-energy Ge recoils of interest in this experiment. The pulsed nature of the neutron beam, with 2-ns width and 400-ns period, together with its monochromaticity, allowed the use of time-of-flight (TOF) constraints to reduce the accidental background that would otherwise bury the recoil signal. The profile of neutron beam energy E_{n} was determined for each measurement period using the neutron TOF from their production at the Li target to their interaction in an 2"-diameter, 2"-length EJ-309 liquid scintillator [1] cell placed at a known distance. The beam energy distribution followed a narrow Gaussian shape, whose mean and rms values are presented in table 2.1.

The Ultra-LEGe (aka, ULEGe) detector active volume was carefully aligned with the approximately 30 mm x 30 mm beam cross-sectional area at about 100 cm from the ^{7}Li target. The germanium active volume position within the detector aluminum cap was estimated from the detector drawings provided by the manufacturer. The target thickness and beam current were kept small (870 nm and 580 nA for the October 2017 runs) in order to generate a low the beam flux (40 $\mathrm{n/cm^2/s}$ for the October 2017 runs) and thus, limit the radiation damage produced by neutrons to the germanium crystal. However, during the course of this experiment, the intrinsic detector electronic noise grew from 74 eV FWHM (October 2017) to 95 eV FWHM (March 2018).

Twenty seven 2"-diameter, 2"-length EJ-309 liquid scintillator cells were used as backing detectors. The use of PSD capable EJ-309 [11] enables accidental gamma background rejection. Also to reduce the gamma background contamination, the liquid scintillator aluminum cases were covered with 1-mm thick lead sheet envelops.

Initial toy simulations showed that the expected flux of neutrons scattering from the germanium into a 2"x2" angular bin (1 meter away from the germanium), representing a single backing detector active area, was expected to be of the order of few neutrons per hour, mainly due to the small germanium detector size. Thus, the backing detectors were attached to a frame configured as two concentric annuli with 8 and 19 backing detectors each and of 294 mm and 452 mm respective radii, as shown in figure 2.1[1]. With the frame plane situated perpendicular to the neutron beam, and

[1]The channel corresponding to detector 26 in the diagram of figure 3.1 was not instrumented.

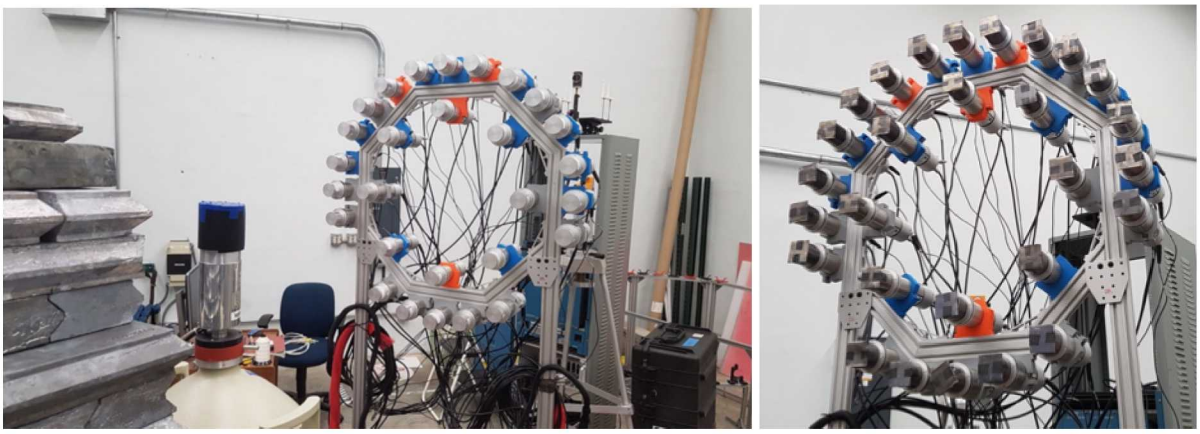

Figure 2.1. Experimental setup at TUNL: the left photo shows the ULEGe detector and the backing detector frame; the right photo shows the backing detectors with the lead sheet caps.

the annuli center co-lineal with the Li target and the germanium volume, all the backing detectors of a given annulus were intended to record the same neutron scattering angle. Therefore, only two germanium recoil energies were probed for any given ULEGe-frame distance, and the contribution of the individual backing detectors of the same annulus can be added together. In reality, a narrow distribution of germanium recoil energies is expected, mainly due to the backing detectors finite size and the beam energy spread. Table 2.1 lists the selected ULEGe-frame distances d for five data runs. The frame distances d and beam energies $E_{\rm n}$ were intentionally chosen to closely overlap some of the recoil energies $E_{\rm nr}$ probed by the inner annulus detectors of one run with the energies probed by the outer annulus detectors of a different run, as a check on systematic effects.

The ULEGe detector high-voltage was supplied via a Canberra 3160D NIM high-voltage power supply. A Canberra 2016 NIM spectroscopy amplifier provided the detector preamplifier power and shaped the preamplifier output pulse with 12 μs shaping time, for which the shaped pulse peaked at $\sim 24\mu$s. The backing detectors were gain matched using a ^{137}Cs source. Two Struck SIS3316 digitizers [2] were used to digitize all the detectors pulses as well as the pulse from the beam-pickoff monitor (BPM) system, at a 250 MHz sampling rate. About 40 μs of the germanium shaped pulse output were digitized, corresponding to a 10,000 sample waveform. Four hundred nanosecond waveforms were saved for each backing detector and the BPM channels. Each backing detector channel was allowed to individually trigger for signals above a low hardware threshold; the individual channel internal trigger was then routed out to generate an external trigger for the two digitizers, and all channels were synchronously recorded with one common timestamp.

Absent from Table 2.1 is the September 2017 measurement period. Two runs were performed during that first period: one for frame distance d = 101.0 cm, $E_{\rm nr}^{\rm inner} \sim 0.61$ keVnr, $E_{\rm nr}^{\rm outer} \sim 1.33$ keVnr, and another one for d = 154.9 cm, $E_{\rm nr}^{\rm inner} \sim 0.27$ keVnr, $E_{\rm nr}^{\rm outer} \sim 0.61$ keVnr. The analysis of the much lower ionization energies resulting from those runs will require a more careful treatment than for the remaining datasets, and thus, will be addressed in a later analysis stage.

	Oct 2017			Feb 2018	Mar 2018
Run label	1	2	3	4	5
$d[cm]$	75.06	83.00	89.60	75.60	83.20
E_{n} [keV]	617.9	617.9	617.9	1320.4	1314.5
$E_{\mathrm{n}}^{\mathrm{rms}}$ [keV]	11.3	11.3	11.3	13.6	12.7
$E_{\mathrm{n}}^{\mathrm{sys}}$ [keV]	1.8	1.8	1.8	5.3	4.0
Inner Annulus					
E_{nr} [keVnr]	1.111	0.932	0.813	2.375	2.007
	($\pm$0.038)	($\pm$0.032)	($\pm$0.028)	($\pm$0.089)	($\pm$0.082)
TOF min [ns]	360.4	367.0	372.4	329.6	332.0
TOF max [ns]	383.3	391.2	398.2	346.8	350.2
Outer Annulus					
E_{nr} [keVnr]	2.317	1.978	1.745	4.907	4.27
	($\pm$0.036)	($\pm$0.031)	($\pm$0.027)	($\pm$0.075)	($\pm$0.065)
TOF min [ns]	364.7	370.7	374.9	330.43	332.90
TOF max [ns]	387.1	395.2	404.1	352.0	350.3

Table 2.1. Columns are labeled by the run index. Top section rows: ULEGe-frame distance and neutron energy distribution parameters. Middle and bottom section rows: the expected recoil energy derived from simulations and the TOF coincidence ranges, for the inner and outer annulus detectors respectively.

Chapter 3

Simulations

A Monte Carlo model of the experimental setup was constructed using Geant v4.10.01.p02, [4]. The ULEGe internal geometry, modeled in detail using the dimensions and materials according to the manufacturer drawings, is depicted in figure 3.1. Of most relevance for this simulation is the 9.5-mm thick aluminum top lid surrounding and in close proximity to the germanium element, which acts as a neutron scattering material creating background contamination in the germanium spectra, as will be shown below. Each backing detector was modeled as a 1-mm thick aluminum cylindrical cell with a 1-mm thick acrylic window on one side, filled with EJ-309 liquid scintillator. Lead cylindrical caps of 1.6-mm thickness cover the front and cylindrical faces of each backing detector; these are slightly different from the actual lead caps used in the experiment, in which the flat front sheet is squared shaped instead of circular. The germanium crystal was centered at the coordinate origin. Eight backing detectors were equidistantly arranged in an annulus of radius 294 mm, measured from the center of the backing detector cylinder. The remaining nineteen backing detectors were arranged along a second co-centric annulus of radius 452 mm, most of them angularly separated by $1/24 \cdot (2\pi)$, with few wider angular gaps matching the experimental setup shown in figure 2.1. The two co-planar annuli, shown in figure 3.1 (right) with the detector ID numbering scheme, are perpendicularly centered in the y axis. The distance d between the ULEGe detector and the annuli plane, measured from the germanium center to the plane containing the lead caps front, was adjusted according to the experimental run being simulated. Neutrons are emitted towards the ULEGe detector from the opposite side of the y axis as a parallel beam of 30 mm x 30 mm cross sectional area centered in the y axis. The simulated beam neutron energies were sampled from Gaussian distributions with the experimentally determined means and rms listed in Table 2.1.

Neutron interactions are modeled by the `QGSP_BERT_HP` physics list, which includes high precision hadronic models for energies below 20 MeV based on reaction cross section and elastic scatter angular distributions experimental data. For the proton recoils in EJ-309, we use the energy-dependent proton light output $L = 0.634E_p - 1.45\left[1 - \exp\left(-0.427E_p^{1.050}\right)\right]$, measured in [15], where L is expressed in keV electron-equivalent (keVee) units and E_p is the proton recoil kinetic energy measured in keV. Data collected with a ^{137}Cs source placed in front of the backing detector frame was used, in conjunction with the simulation of this setup, to determine the energy Gaussian resolution broadening $\sigma_{\mathrm{BD}} = \frac{E}{2.355}\sqrt{(\alpha^2 + \frac{\beta^2}{E} + \frac{\gamma^2}{E^2})}$ of each individual backing detector cell, where E is in keVee. Figure 3.2 shows the fit of the ^{137}Cs data to their smeared-energy simulation histogram for one inner-annulus and one outer-annulus detector. These experimental data were also used to determine the backing detector's keVee energy calibration, and correspondingly, to establish the keVee value of the backing detector threshold applied in the data analysis.

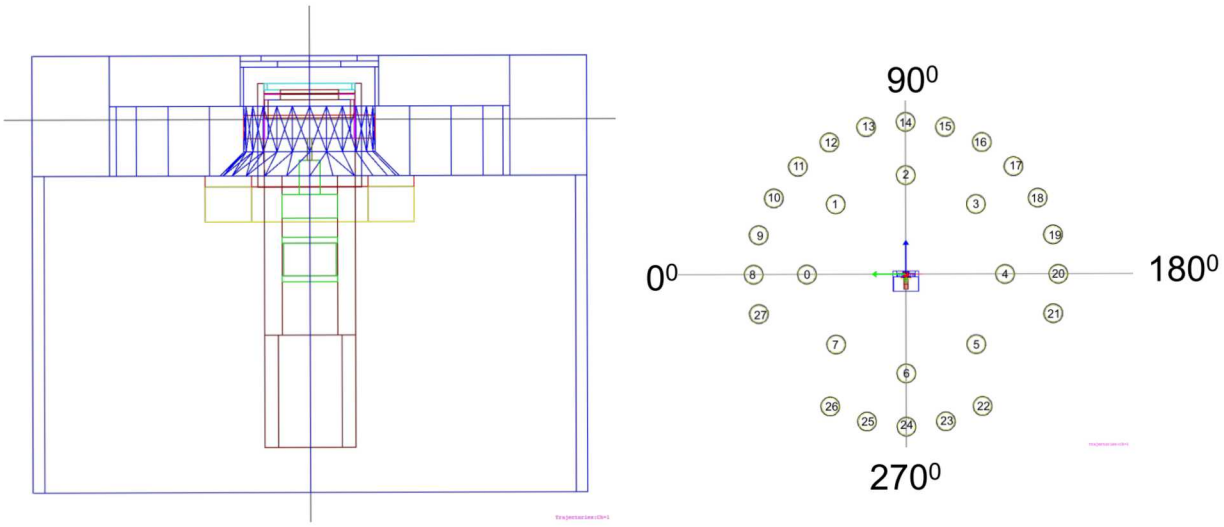

Figure 3.1. Left: simulated ULEGe geometry according to the manufacturer-provided technical drawings. Right: simulated backing detector frame configuration.

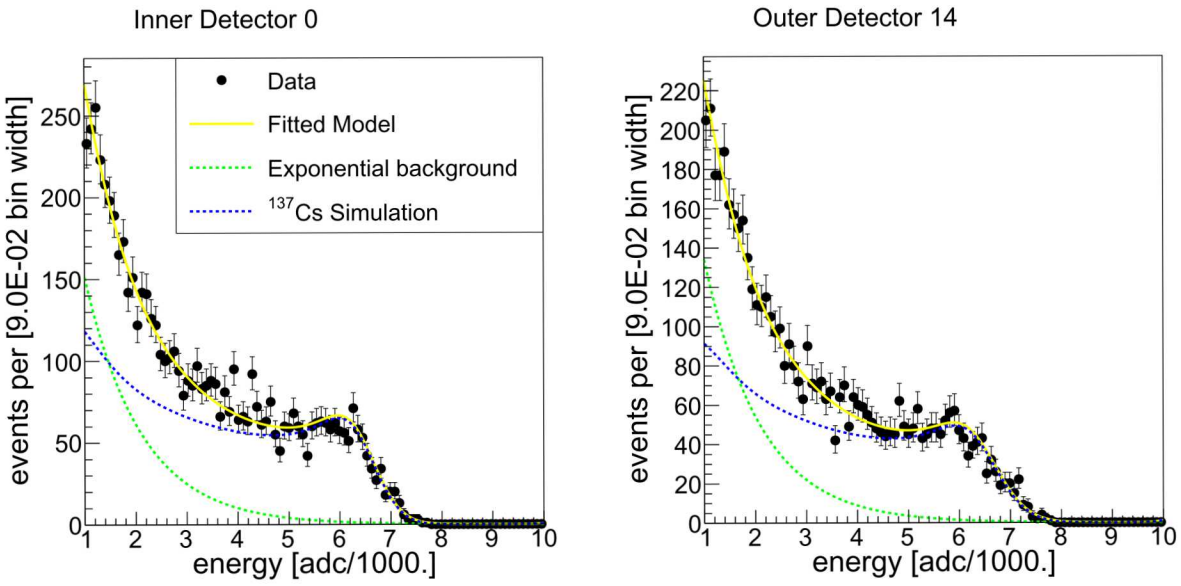

Figure 3.2. Backing detector ^{137}Cs spectra and corresponding fits for one inner detector (left) and one outer detector (right).

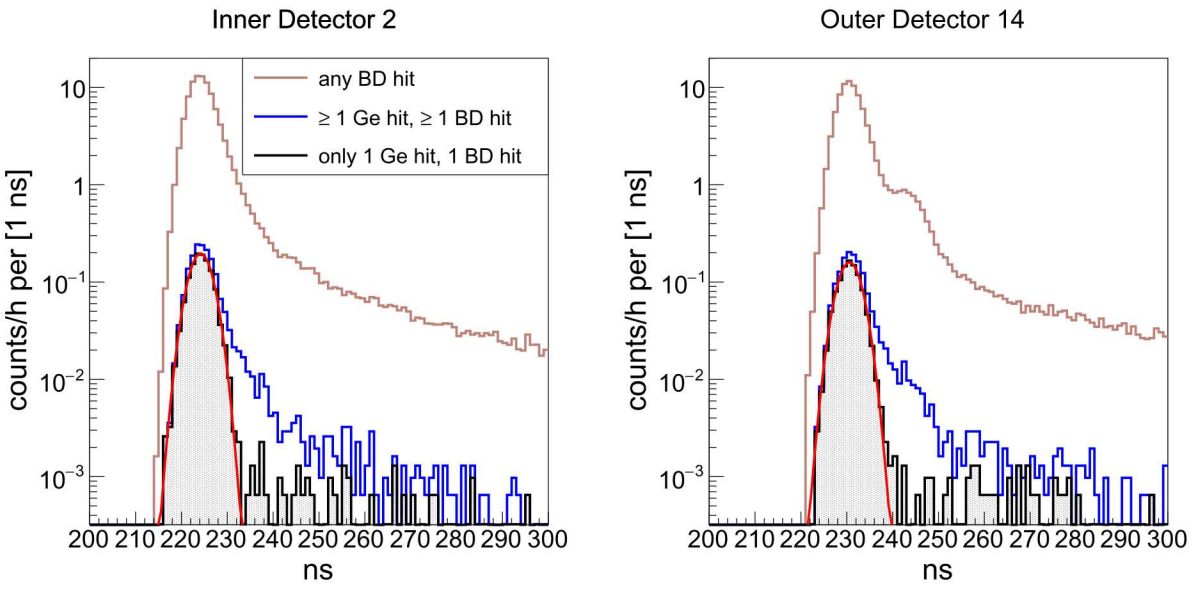

Figure 3.3. Simulated neutron TOF from their emission to their first interaction in one inner detector (left) and one outer detector (right), for run 1 configuration. Black: events where the neutron only scatters in the germanium and then in the backing detector. Blue: events where the neutron scatters at least once in the germanium and at least once in the backing detector, not excluding events with scatters also in the surrounding materials. Brown: all events where the neutron scatters in the backing detector.

Figure 3.3 shows the simulation histograms of the neutron TOF from their emission to their first interaction in one inner annulus detector and one outer annulus detector, for the experimental run 1 settings, where a 37 keVee threshold was applied to the smeared energy deposited in the liquid scintillator matching the experimental threshold. Events where there is at least one neutron interaction in the germanium crystal constitute $< 2\%$ of the above-threshold backing detector hits, evidencing that the materials surrounding the germanium crystal cause most of the neutrons scatters registered by the backing detectors. Furthermore, events where the neutrons scatter not only in the germanium crystal but also in other surrounding materials create non-gaussian right-sided tails in the TOF energy distribution (as also observed in data, see figure 4.1). These conclusions were verified by simulating the bare germanium crystal while maintaining the full backing detectors geometry, as well as by simulating only the germanium and the liquid scintillator active volumes. Hence, we select a TOF coincidence window centered in the TOF Gaussian distribution corresponding to events where the neutrons only scatter in the germanium and in the backing detector—the black-shaded histogram in figure 3.3 fitted by the Gaussian function depicted in red—and assign a TOF window width equal to 2x3 times the Gaussian standard deviation. As will be discussed in section 4, this motivates the selection of the experimental TOF coincidence window.

Germanium recoil energy histograms corresponding to the simulation of run 1 are plotted in

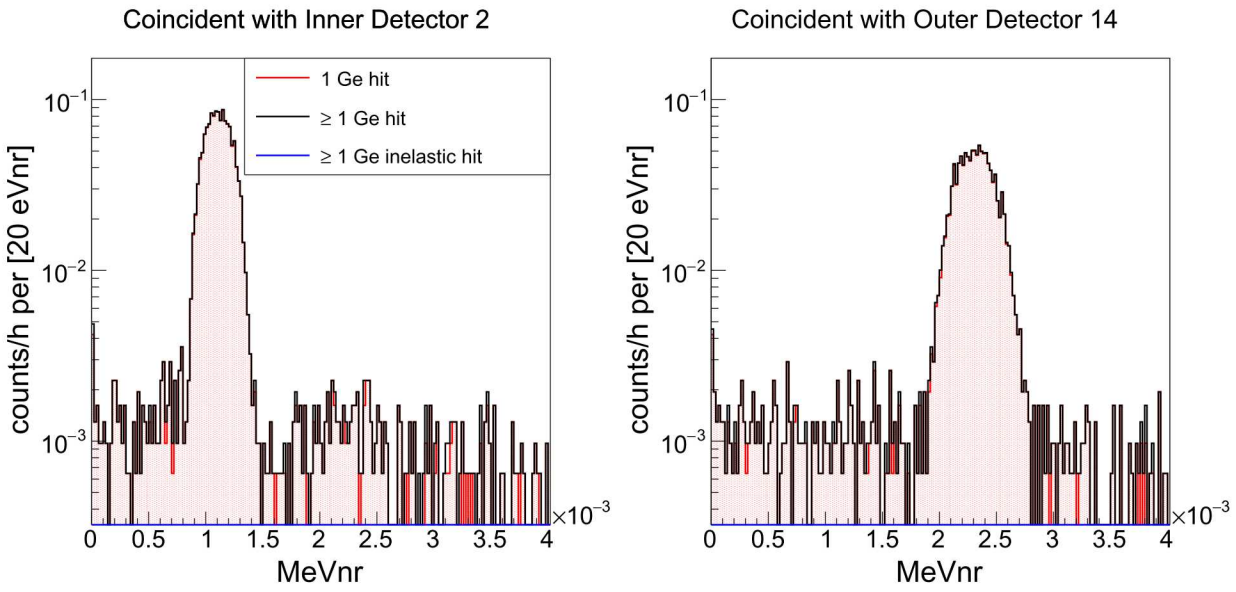

Figure 3.4. Simulated germanium recoil energy histograms for one inner detector (left) and one outer detector (right), for run 1 configuration. Red: only one neutron scatter in germanium. Black: one or more neutron scatters in germanium. Blue: one or more neutron inelastic scatters in germanium.

figure 3.4 for one coincident inner-annulus detector and one coincident outer-annulus detector, illustrating the narrow range of germanium recoil energies E_{nr} (expressed in MeV nuclear-recoil or MeVnr) probed by each annulus detector set. The fraction of coincident events containing more than one neutron scatter in the germanium element is $< 1\%$, and thus, negligible as expected. A continuous and small background contribution appear due to germanium recoils generated by neutrons that have previously scattered in other surrounding materials. Recoils due to neutron inelastic interactions with germanium are negligible for beam neutron energies < 1 MeV; however, for the higher beam energies of runs 4 and 5, the inelastic background contribution increases, though still at negligible levels.

Figure 3.5 shows the number of germanium recoils with energy in the range 0-4 MeVnr, normalized by simulated time, versus the 2D annulus angular position (see figure 3.1) of the backing detector that registers the first above-threshold neutron interaction within the TOF coincidence window. For all the simulated runs, the scattering rate per detector varies according to the density of materials surrounding the germanium; e.g., detectors near the horizontal plane (at 0^o and 180^o) receive less germanium-scattered neutron compared to detectors at $\sim 90^o$, mainly due to the thick aluminum lid surrounding the germanium element cylindrical side. As a check, similar plots for the bare germanium element simulation do not show a rate dependance on the backing detector positions within their respective annulus.

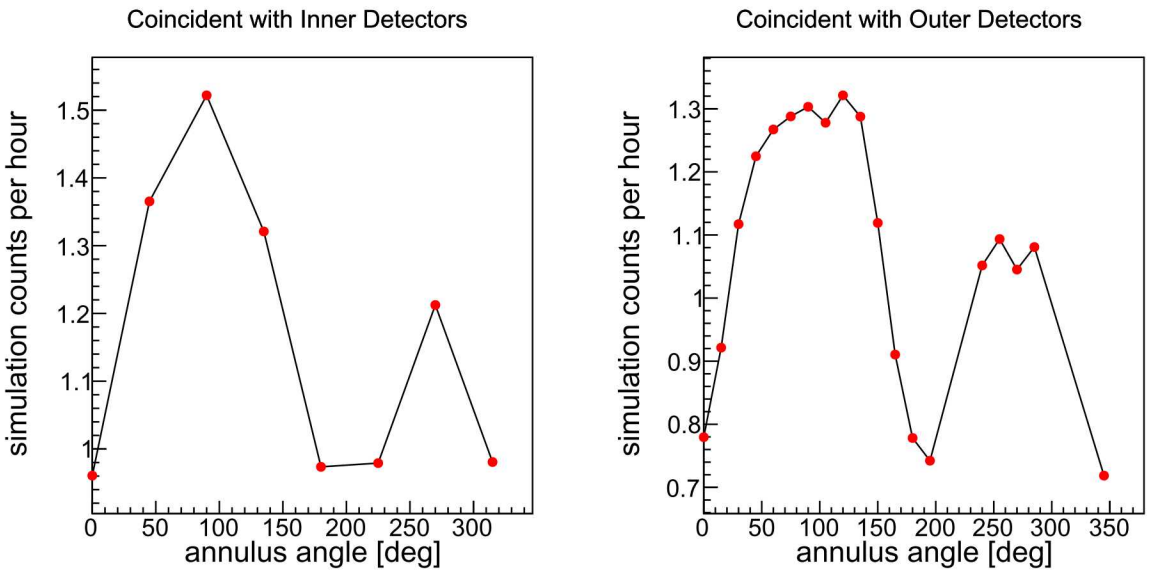

Figure 3.5. Simulated germanium recoil rate for the inner detectors (left) and the outer detectors (right), for run 1 configuration.

Chapter 4

Data Processing

Germanium-scattered beam neutrons generating backing detectors signals are selected via pulse-shape discrimination (PSD), and by requiring TOF coincidence within a given time window. Since the backing detector gains were closely matched, a common 500 adc-units analysis threshold—equivalent to $\sim$ 37 keVee—was applied to all backing detector channels.

Figure 4.1 shows the histograms of the time from the BPM trigger to the backing detector pulse onset—*i.e.*, the experimental TOF—after applying neutron PSD, for all inner-annulus detectors and all outer-annulus detectors of run 1. As expected from the discussion in section 3, the neutron TOF distribution contains a right-sided tail due to beam neutron scatters in surrounding materials. Motivated by figure 3.3, we thus fit a Gaussian to the rising edge of the TOF distribution, and, for each annulus, select a TOF window centered at the Gaussian mean and with a width equal to 2x3 times the standard deviation. The resultant TOF coincidence windows selected this way are listed in Table 2.1 for run 1 and all other runs.

The germanium ionization energy is extracted from the maximum sample value of the germanium digitized shaped pulse, without subtracting the baseline. The conversion from digitizer to energy units near the sub-keV region was derived, for each run, from the ULEGe exposure to a ^{55}Fe source which emits two X-rays of 5.899 keV and 6.49 keV, and from the internal decay of neutron-activated ^{71}Ge which produces a 10.3664 keV peak. We also include a zero-keV point corresponding to the mean of the waveform sample value distribution, *i.e.*, the germanium waveform baseline value. Figure 4.3 (left) demonstrates the excellent linearity of the digitizer-to-keV calibration during all all data runs of the experiment. The above datasets are also used to derive the germanium detector electronic noise σ_{elec} and Fanno factor F [12], which are related to the measured peak energy resolution via the formula $\sigma^2 = \sigma_{elec}^2 + F\varepsilon E$, where σ is the peak standard deviation, and $\varepsilon = 2.96$ eV. The plots of figure (4.3, right), where the zero-keV intercept corresponds to σ_{elec}, show an increase in electronic noise in the later data runs due to the crystal damage caused by neutron irradiation. Moreover, the energy resolution of the neutron activation peak does not follow the expected resolution energy dependence. Since we are interested in the $<\sim 1$ keV region , we will only use the baseline and ^{55}Fe data points to derive the energy resolution parameters σ_{elec} and F relevant at those energies.

The last signal cut to consider is illustrated by the 2D histograms of the calibrated germanium ionization energy versus the time of the germanium waveform maximum sample, t_{peak}, plotted in figure 4.3 for run 1. As these histograms show, the germanium recoil waveforms peak at around

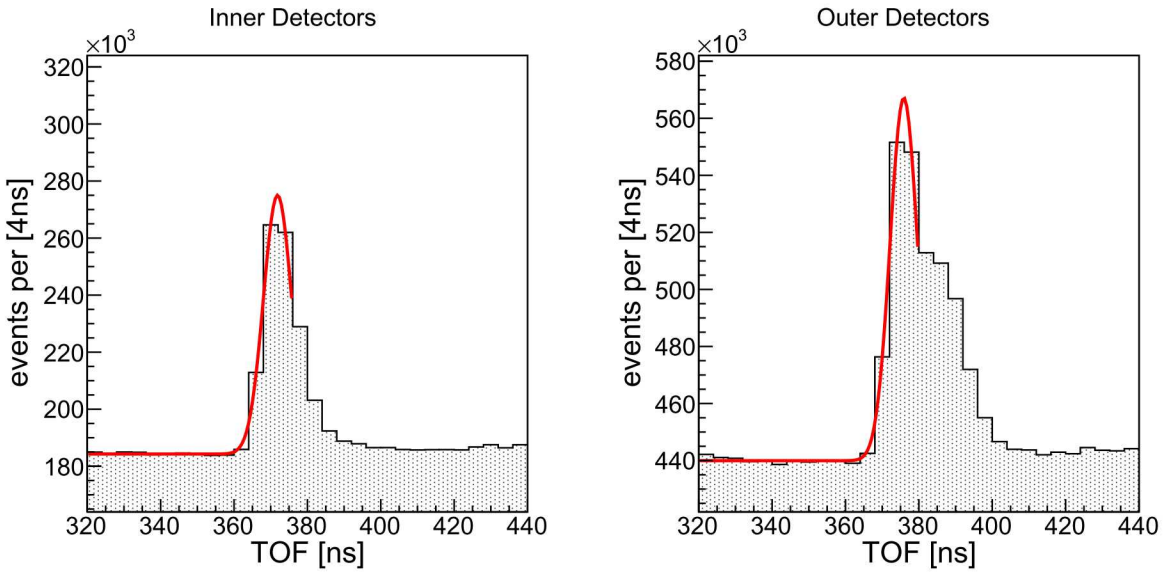

Figure 4.1. Experimental neutron TOF from the BPM trigger to the backing detector pulse onset for one inner detector (left) and one outer detector (right) of run 1. The Gaussian fit of the rising edge of each TOF distribution is presented in red.

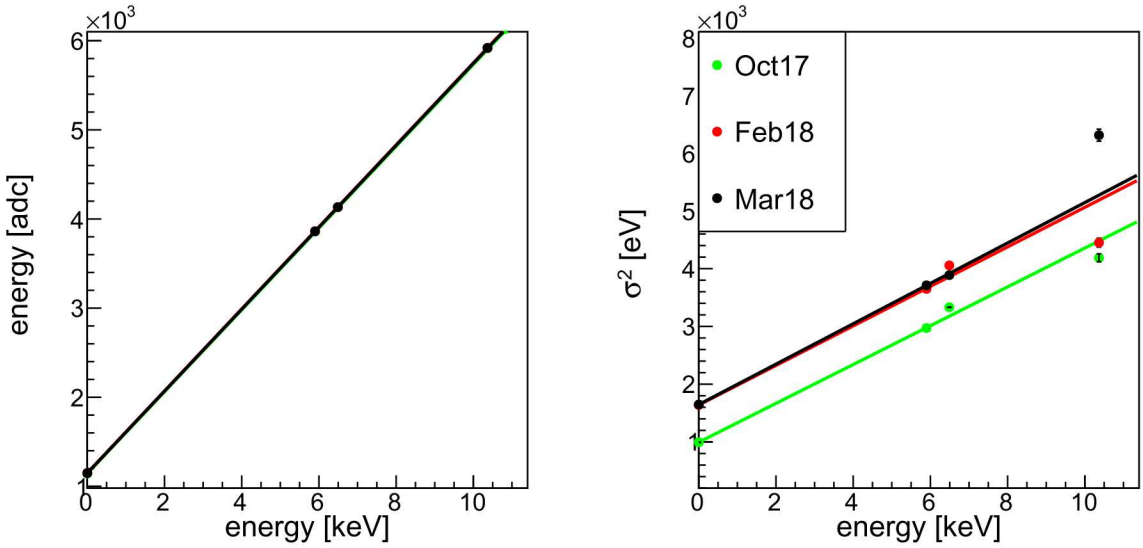

Figure 4.2. Left: adc-to-keV calibration data and fit for the ULEGe detector. The adc energy values of the Oct17, Feb18 and Mar18 data runs are all plotted but closely overlap. All da Right: resolution vs.energy data and fit for the ULEGe detector.

	October 2017	February 2018	March 2018
gain $[\frac{\text{keV}}{\text{adc}}]$	0.002179	0.002174	0.002175
offset [keV]	-2.4935	-2.5001	-2.4985
σ_{elec}[keV]	0.03155	0.04049	0.04059
Fanno factor F	0.11356	0.11560	0.11814

Table 4.1. ULEGe energy calibration and resolution values.

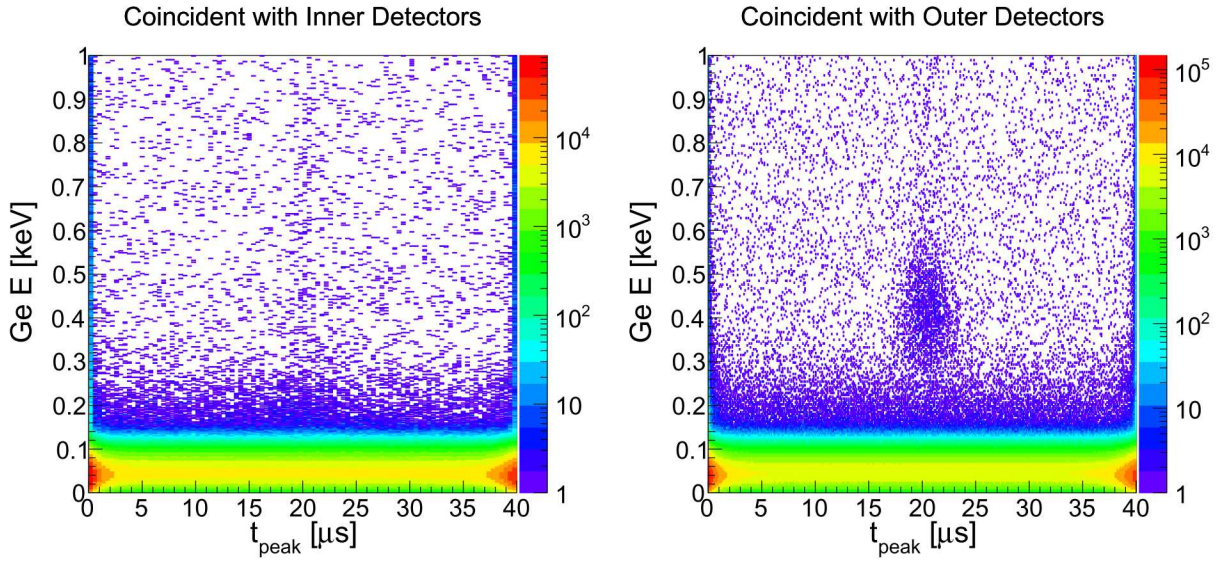

Figure 4.3. Germanium ionization energy vs. germanium waveform peaking time for one inner detector (left) and one outer detector (right) of run 1.

$t_{peak} \sim 20\ \mu$s, compared to background events. The latter are mainly due to electronic noise, and thus, their maximum sample values can randomly occur any time in the waveform. Taking this into account, figures 4.4–4.8 present the germanium spectra of each run, when there is at least one backing detector above-threshold neutron signal within the corresponding TOF coincidence window, and the germanium peaking time is within the range $t_{peak} = [16.6, 24.6]\,\mu$s. In most runs, the germanium recoil spectra due to events in coincidence with the inner annulus backing detectors overlap with the background pedestal, and thus, an accurate estimation of the background is necessary in order to separate the recoil signal contribution.

In order to estimate the germanium spectra background, we apply TOF and t_{peak} cuts that exclude the germanium recoil signal but maintain the same background spectral shape. Figure 4.9 shows the TOF vs.t_{peak} 2D-histograms of the run 1 dataset, where the parameter region corresponding to the germanium recoil signal is delineated in black, and several *anti-signal* regions are

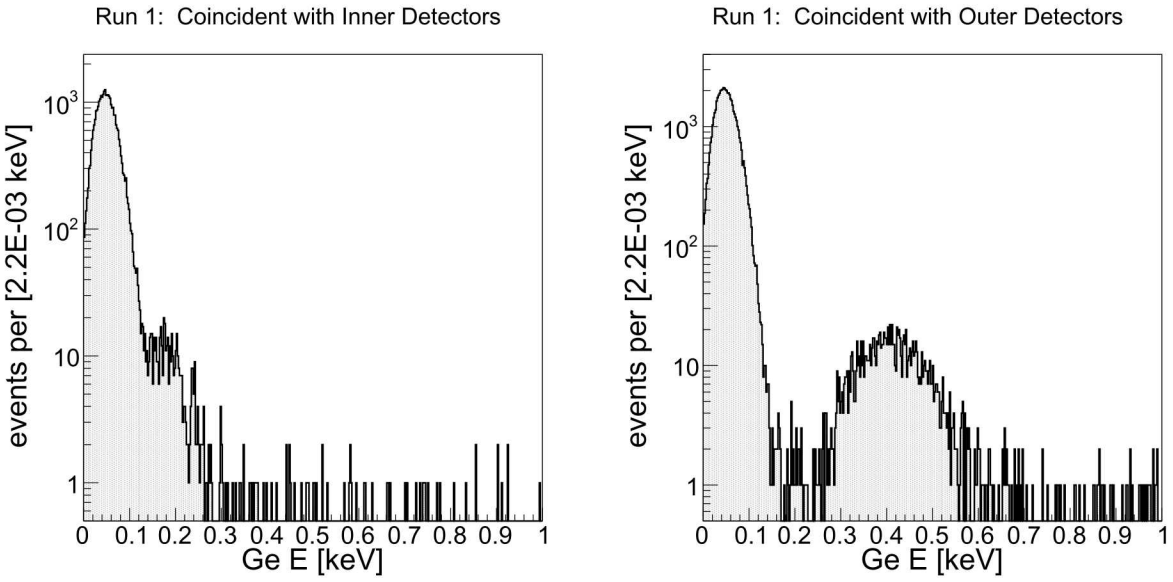

Figure 4.4. Run 1: Germanium ionization energy spectra after all signal cuts for one inner detector (left) and one outer detector (right).

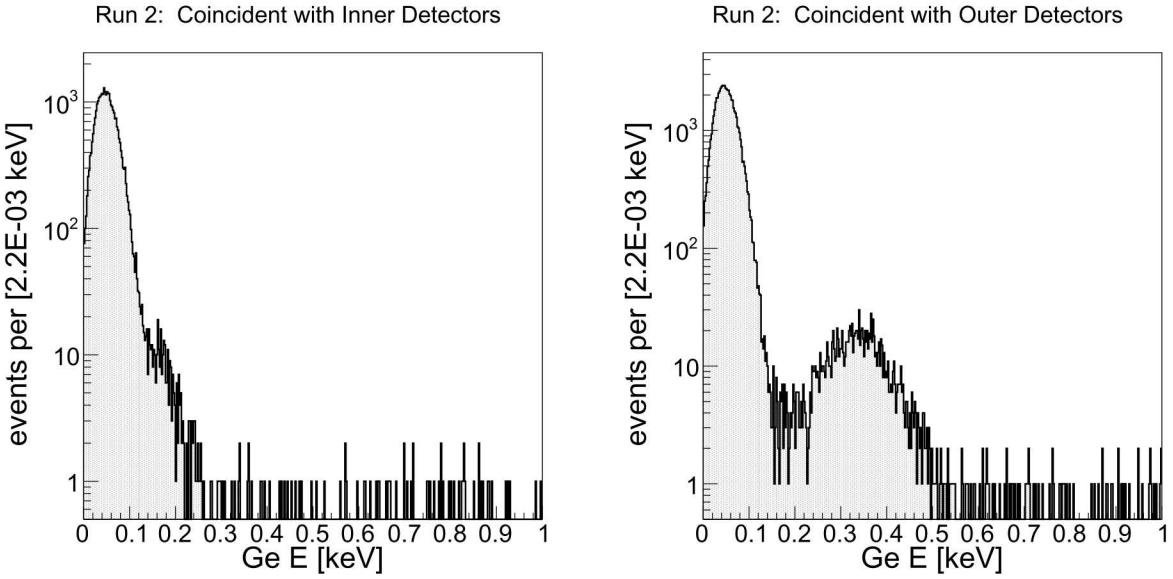

Figure 4.5. Run 2: Germanium ionization energy spectra after all signal cuts for one inner detector (left) and one outer detector (right).

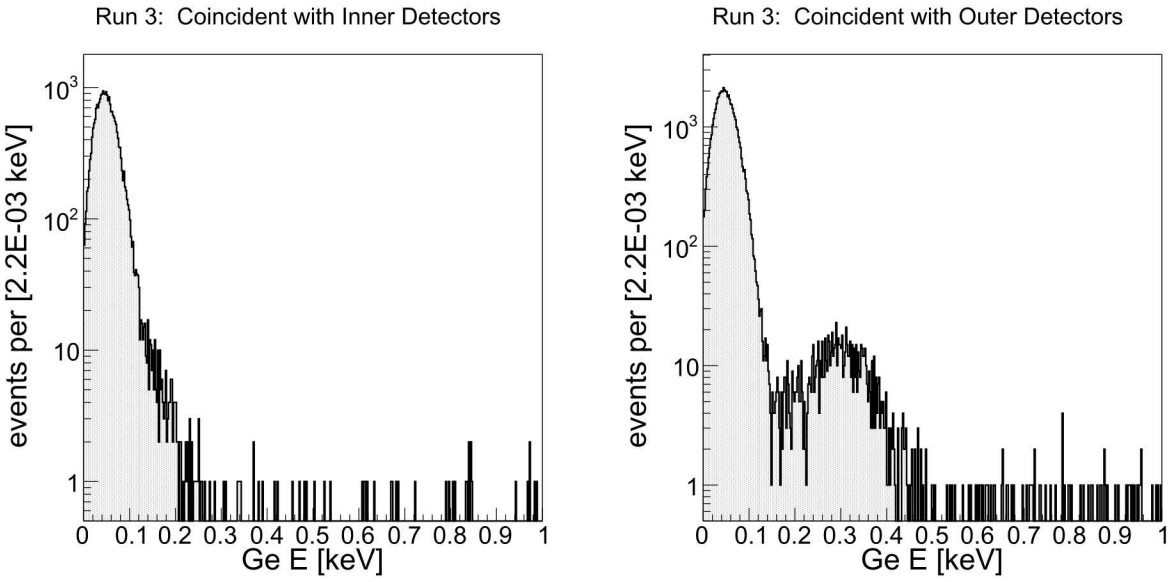

Figure 4.6. Run 3: Germanium ionization energy spectra after all signal cuts for one inner detector (left) and one outer detector (right).

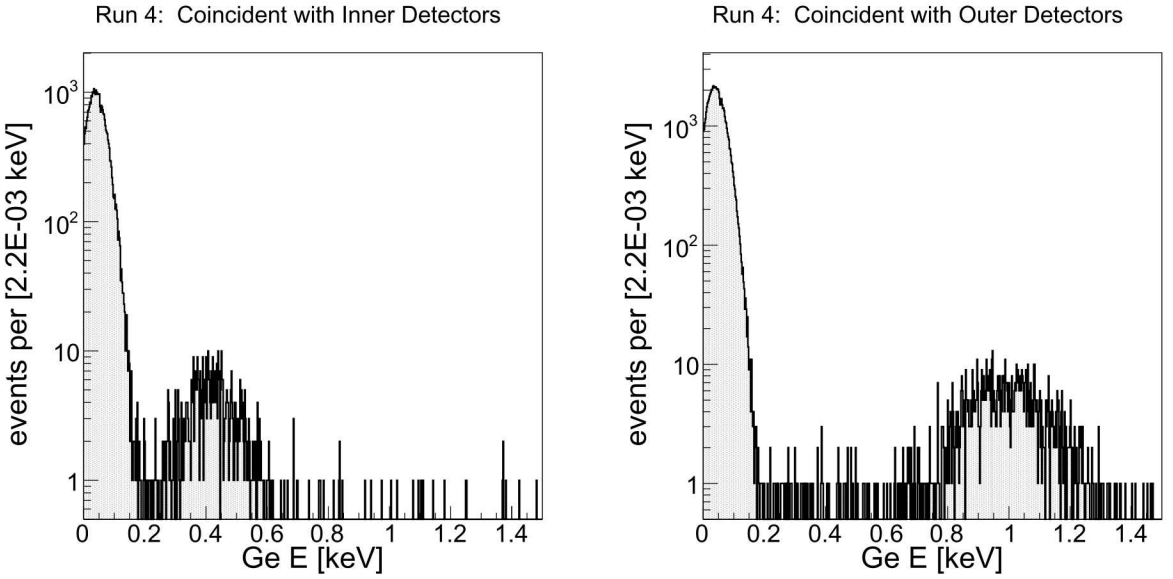

Figure 4.7. Run 4: Germanium ionization energy spectra after all signal cuts for one inner detector (left) and one outer detector (right).

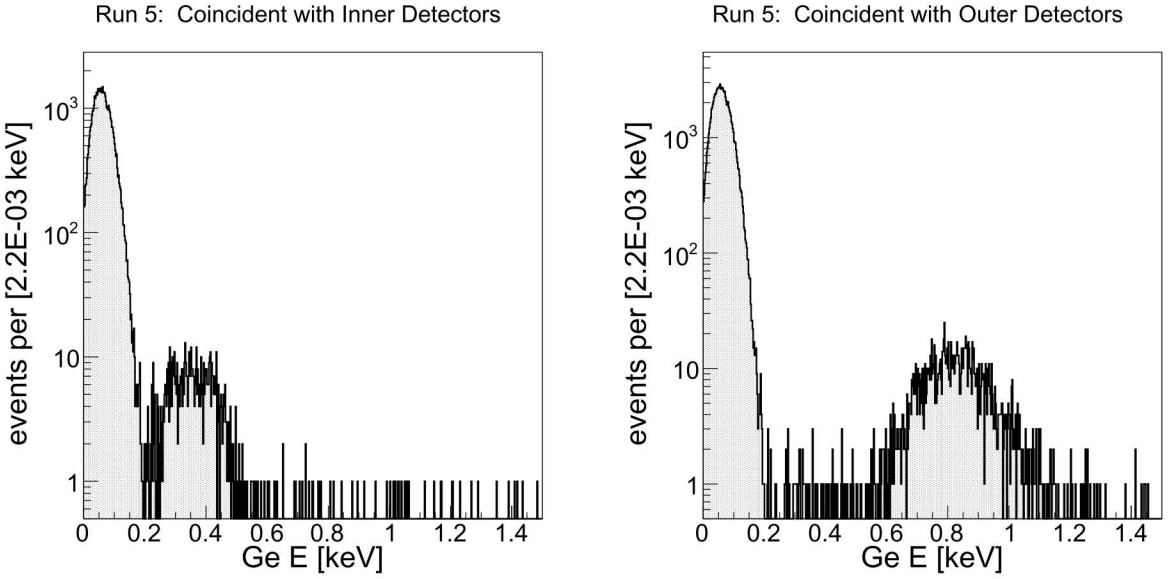

Figure 4.8. Run 5: Germanium ionization energy spectra after all signal cuts for one inner detector (left) and one outer detector (right).

delineated in red. As shown in figure 4.10, the normalized spectra of the different cuts follow the same spectral shape, and thus, we use their normalized sum as the estimation of the germanium spectra background.

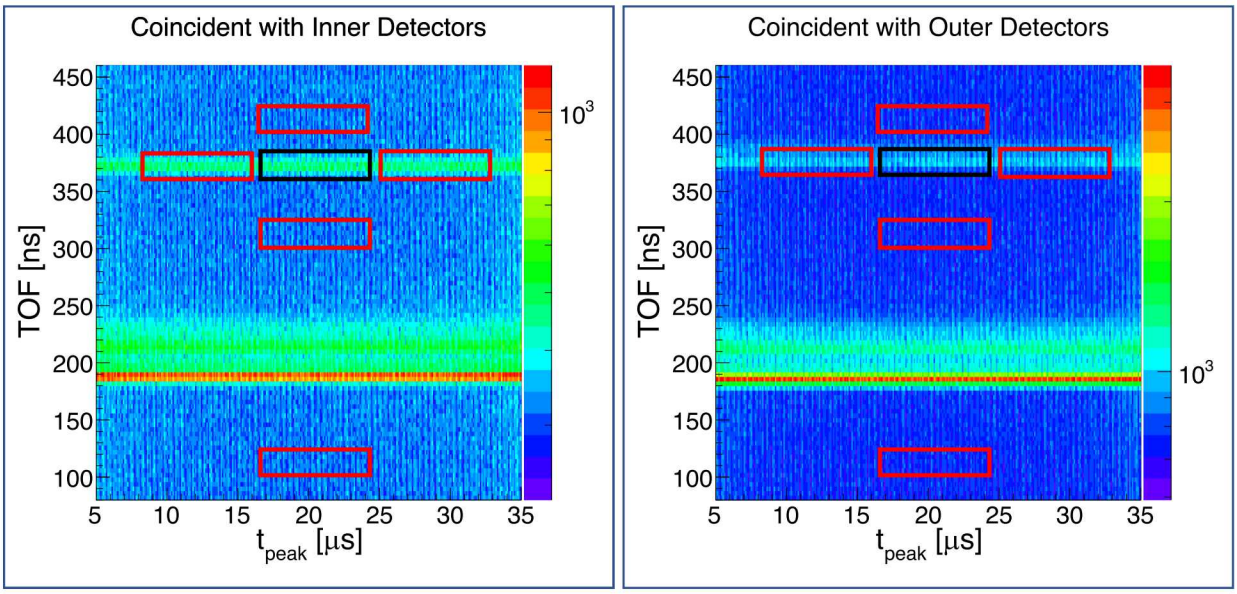

Figure 4.9. Experimental neutron TOF vs. germanium waveform peaking time for one inner detector (left) and one outer detector (right) of run 1. Black delineated area: signal cut. Red delineated areas: *anti-signal* cuts.

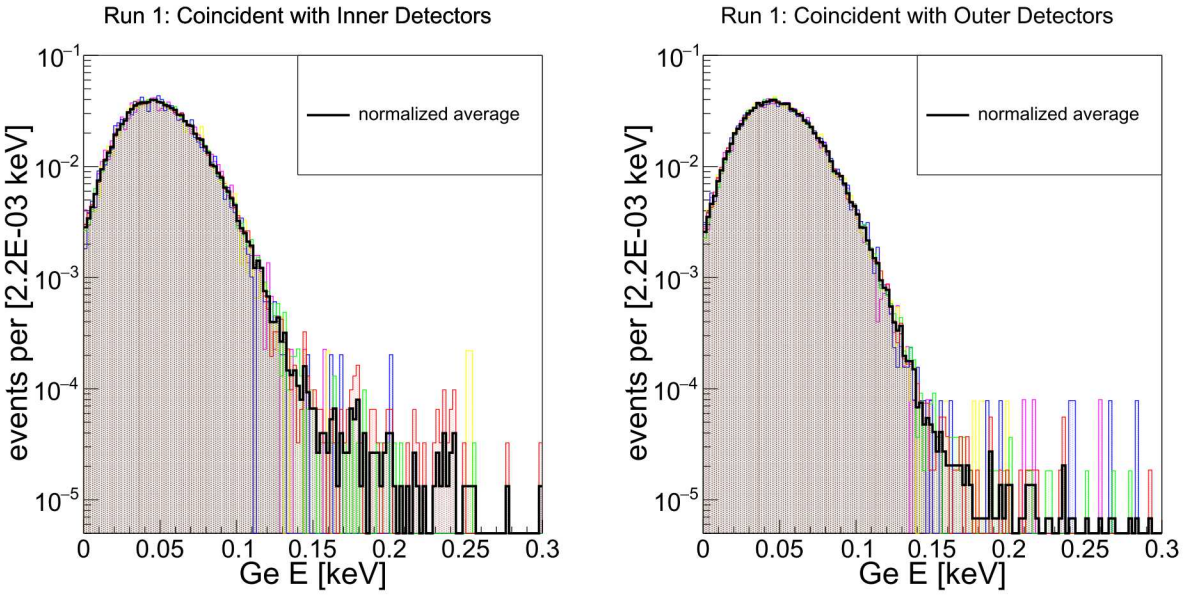

Figure 4.10. Normalized germanium ionization energy spectra for the *anti-signal* cuts of figure 4.9, for one inner detector (left) and one outer detector (right) of run 1. Black only: normalized average of all *anti-signal* cuts.

Chapter 5

Quenching Factor Analysis

The quenching factor Q is derived from scaling the simulation recoil spectra to match the experimental ionization spectra. Lindhard theory [13] provides a prescription for modeling the $Q(E_{\mathrm{nr}})$ energy dependence, which is particularly useful when fitting continuous spectrum data [17] by allowing the Lindhard model parameter k to float. In this work, however, each annulus of backing detectors records a narrow range of germanium recoil energies for each ULEGe-frame distance. Therefore, we assume Q to be constant over the signal range probed by each annulus of backing detectors during each data run, and approximate the germanium ionization energy to $E_{\mathrm{ioni}} = Q \cdot E_{\mathrm{nr}}$, where Q is treated as an energy-independent fitting parameter for each dataset. This approximation loses its validity for events with recoil energy far outside the signal ranges targeted in a give data run, which could be the case for events with multiple neutron-germanium scatters and for background events where the neutron has already scattered in surrounding materials; however, as discussed in section 3, contamination from these types of events is expected to be negligible.

After converting the simulated recoil energy E_{nr} to ionization energy E_{ioni}, the later is convolved with the Gaussian resolution $\sigma^2(E) = \sigma_{elec}^2 + F\varepsilon E + \sigma_x^2$. The first two terms of this formula represent the measured ULGe energy resolution, where σ_{elec} and F are listed in Table 4.1. A third resolution term σ_x is introduced to capture other unaccounted sources of noise, and is left as a free parameter. We do not fix the simulation spectra normalization according to the measured beam neutron flux but instead introduce a signal normalization free parameter ζ_{s} that scales the resultant simulation ionization spectra. Next, we add a background term obtained from experimental events satisfying the *anti-signal* cuts as explained in the previous section, and scale it by the background normalization free parameter ζ_{b}.

Our analysis then determines four parameters $\Theta^{(i)} = \left(Q^{(i)}, \sigma_x^{(i)}, \zeta_{\mathrm{s}}^{(i)}, \zeta_{\mathrm{b}}^{(i)}\right)$ separately for each dataset i ($i = [1, 10]$), of which the two normalization factors are treated as nuisance parameters. Although our main purpose is to determine $Q^{(i)}$ for each dataset, we are also interested in understanding the physical origin of $\sigma_x^{(i)}$. For our task, we employ a Markov Chain Monte Carlo (MCMC) algorithm that samples the posterior probability distribution $P\left(\Theta^{(i)} \mid \boldsymbol{n}^{(i)}\right)$ in the $\Theta^{(i)}$ space for the experimental binned data $\boldsymbol{n}^{(i)}$ of each separate dataset i. From Bayes's theorem, the logarithm posterior probability distribution can be written as

$$\ln P(\Theta \mid \boldsymbol{n}) \propto \ln L(\boldsymbol{n} \mid \Theta) + \ln P(\Theta) \tag{5.1}$$

where $L(\boldsymbol{n} \mid \Theta)$ is the likelihood function and $P(\Theta)$ is the parameters' prior probability distribution

[1]. We assume that all parameters are independent and only constrained by our choice of their range, so that $\ln P(\Theta)$ is either 0 or $-\infty$. The binned likelihood function assumes that each data bin j obeys a Poisson distribution of mean μ_j,

$$\ln L(\boldsymbol{n} \mid \Theta) = \prod_j \frac{\mu_j^{n_j} \mathrm{e}^{-\mu_j}}{n_j!} \tag{5.2}$$

where the μ_j represents the simulated ionization spectra bin value for the parameter choice Θ. The sampling of $P(\Theta \mid \boldsymbol{n})$ is done with the **emcee** [8] Python package, which implements the Goodman and Weare's affine invariance ensemble sampler [9].

Parameter	Prior range	Most probable value	RMS
Q	[0.05,0.30]	0.1770	0.0004
σ_x [keV]	[0.028, 0.08]	0.05315	0.00115

Table 5.1. MCMC parameters range and results.

In this report, we present the results corresponding to the outer annulus dataset of experimental run 1. Two separate MCMC chains were generated, each with 10^5 update steps. For one chain, 400 walkers were randomly and uniformly initialized over the Θ parameter space, and the typical value $a = 2$ was chosen for the algorithm parameter controlling the step size. The second chain is effectively longer, with 1000 walkers initialized in a 4-dimensional cube at the center of the parameter space, and with $a = 1.25$. In both cases, the walkers converge to the same region of the parameter space after $\sim 10^2$ steps, as observed in figure 5.1. Also for both chains, the parameter σ_x quickly asymptotes to the longest auto-correlation time of about 96 steps, as can be observed in figure 5.2, and the acceptance fraction settles at 0.41 after $\sim 10^3$ steps.

Figure 5.3 presents the posterior probability distributions projected onto the parameters Q and σ_x, respectively, for the last $9 \cdot 10^4$ steps of each chain, which are well beyond the 10^2-step burning time. These plots verify that both chains converge to the same $P(\Theta \mid \boldsymbol{n})$ distribution, with maximum value at $Q^{\max} = 0.177$ and $\sigma_x^{\max} = 0.05315$ keV. The corner plots of the 2D and 1D distribution projections of all parameters of the first chain (a =2, number of walkers = 400) is presented in figure 5.4, showing that the normalization parameters ζ_{s} and ζ_{b} simply converge to Gaussian-like distributions, maximized at $\zeta_{\mathrm{s}}^{\max} = 0.0255$ and $\zeta_{\mathrm{b}}^{\max} = 5.355$. Figure 5.5 shows the comparison of the experimental signal spectrum with the *expectation* spectrum obtained with the parameters $\Theta^{\max}$ as the sum of the the simulated spectrum and the normalized experimental background data.

The resultant quenching factor $Q = 0.177$, corresponding to the germanium recoil energy $E_{\mathrm{nr}} = 2.317$ keVnr probed by this dataset (experimental run 1, outer annulus), is smaller than the values reported by several other authors ([6], [17], [14], [10],[16]) for measurements at the same liquid nitrogen temperature (77 K). This is illustrated in figure 5.6 extracted from [17], where we

[1] In equation 5.1, we have dropped the superscript (i) indicative of the dataset. In what follows, all parameters and data values should be understood as pertaining to the dataset under analysis.

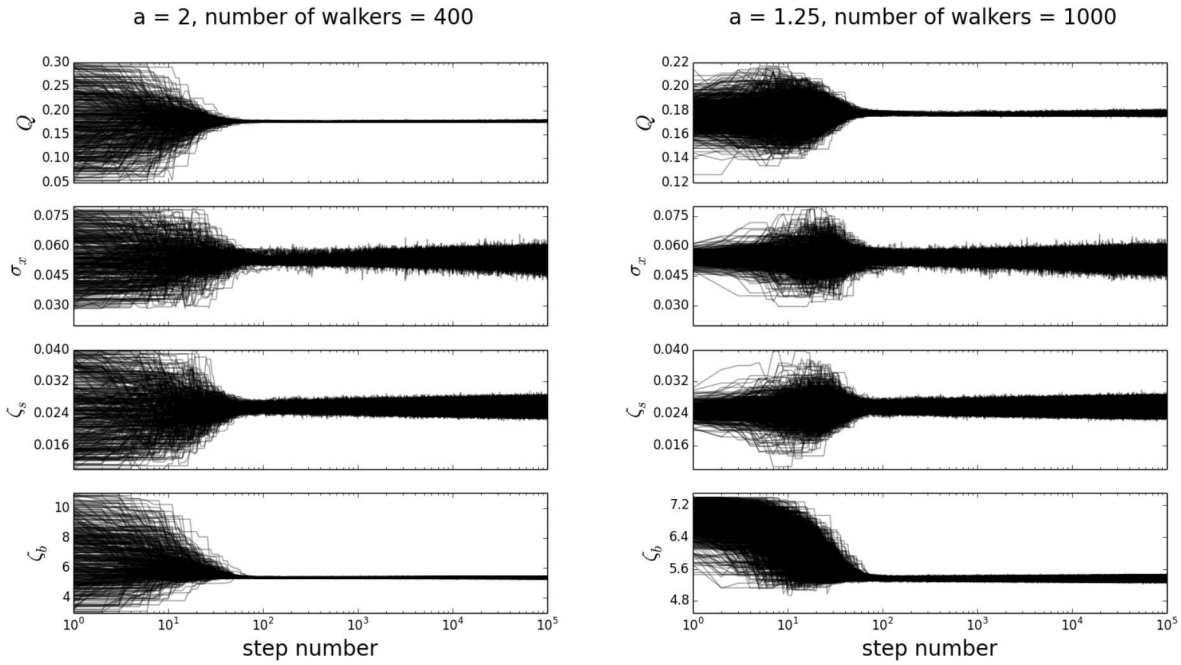

Figure 5.1. Full MCMC chains, each with 10^5 steps.

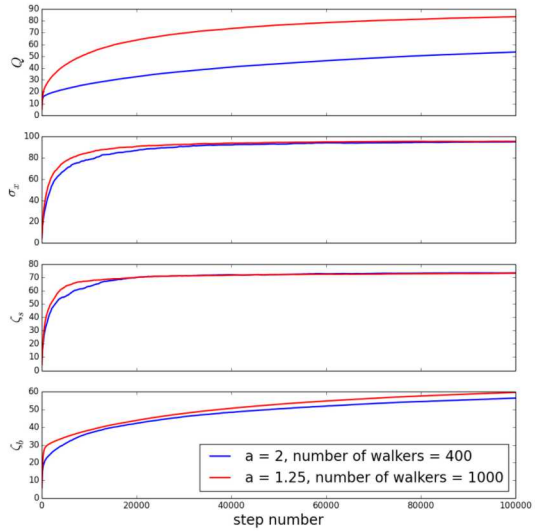

Figure 5.2. MCMC chain autocorrelation time for each model parameter.

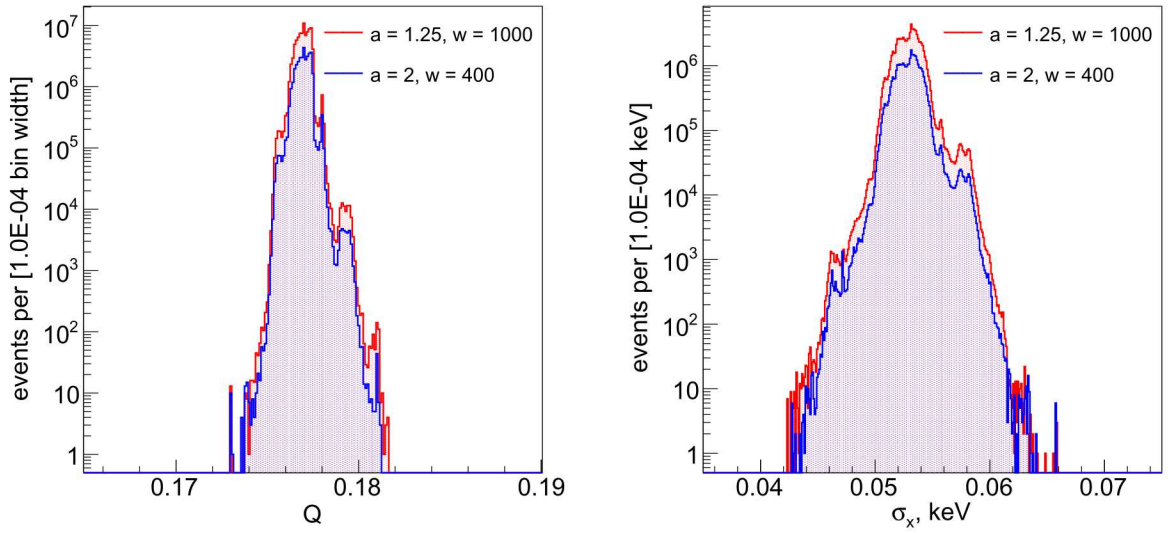

Figure 5.3. The posterior probability distributions projected onto the parameters Q and σ_x, respectively, for the last $9 \cdot 10^4$ steps of each chain.

have also plotted our point $(Q, E_{\mathrm{nr}}) = (17.7\%, 2.317\ \mathrm{keVnr})$. Even though the MCMC processing of the remaining datasets has not yet been finalized, preliminary results show a similar bias towards smaller Q values with respect to the literature values. Incorrect simulated germanium recoil energies could create a systematic error in our derivation of Q. However, in order to explain the possible bias in our data with respect to previously measured Q values, the corresponding bias in the experimental values used as input for the simulation—mainly the neutron beam energy, the ULEGe-frame distance, and the annulus radii—would have to be much larger than their reported errors. A more likely cause could be having an incorrect germanium energy calibration. The calibration values presented table 4.1, however, closely match the values reported by the independent Duke data analysis pipeline suggesting that problems in the calibration, if any, are not likely computational. A revision of our analysis procedures, including the physical model used for the energy quenching, might be necessary if the other datasets result in a consistent deviation from previous literature values.

The value $\sigma_x = 0.05315$ keV obtained for the experimental run 1, outer annulus dataset, is significantly larger than the measured energy resolution—which is about $\sigma \sim 0.034$ keV for E = 0.410 keV = $(0.177 \cdot 2.317)$ keV . Since the fitted experimental spectrum is the sum of the events in all the detectors of a given annulus, one potential cause for the extra smearing could be unaccounted variations in the individual backing detector positions around the annulus circle. For example, rough calculations assuming variations of $\sim 2\%$ ($\sim 5\%$) for the individual backing detector positions, including variations with respect to the annulus plane, produce a smear in the recoil energy mean (converted to ionization energy) of ~ 0.02 keV (~ 0.05 keV). Since the same backing detector frame was used in all runs, it might be possible to verify the consistency of this

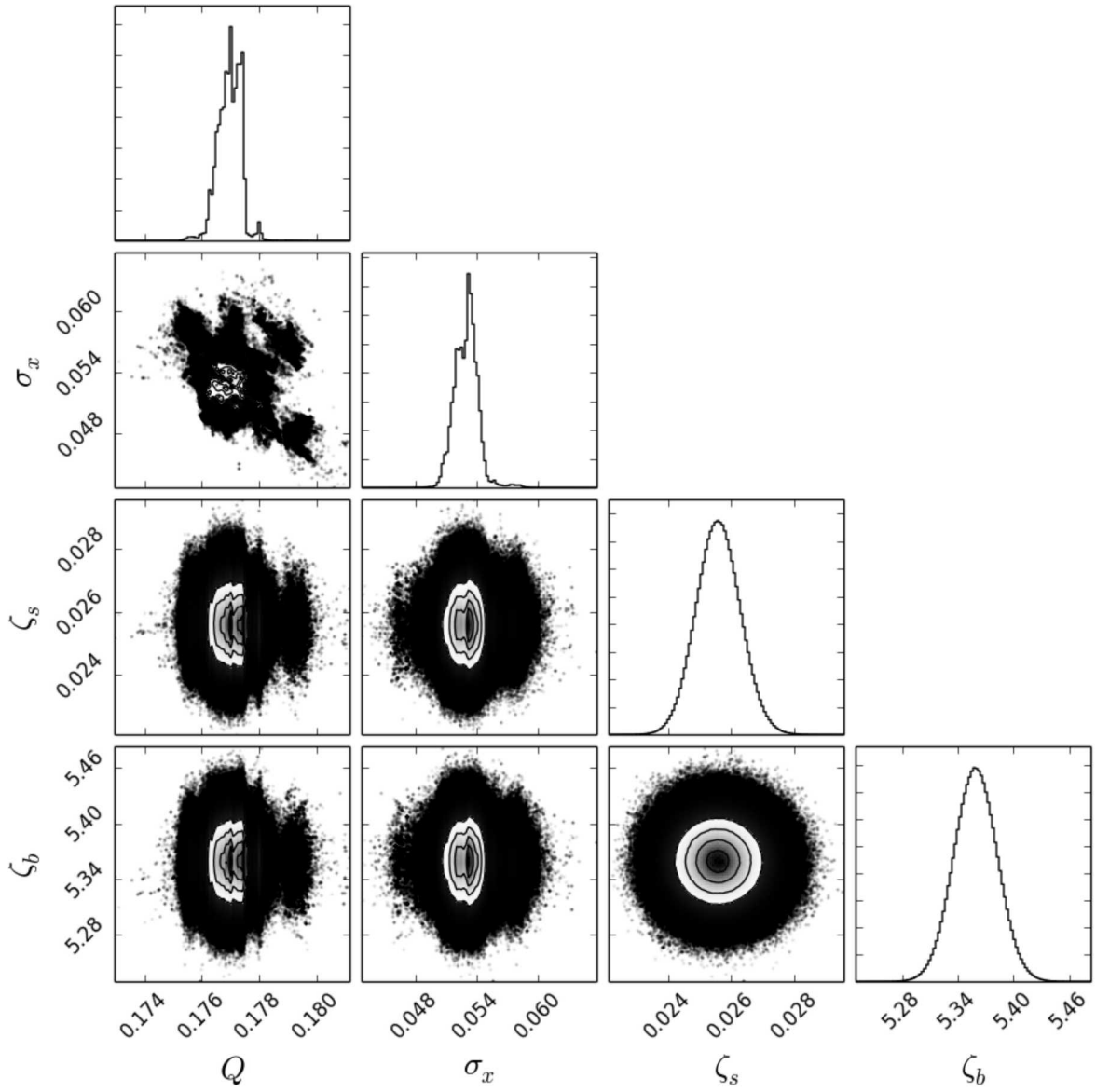

Figure 5.4. Corner plot from MCMC fit showing correlations between parameters.

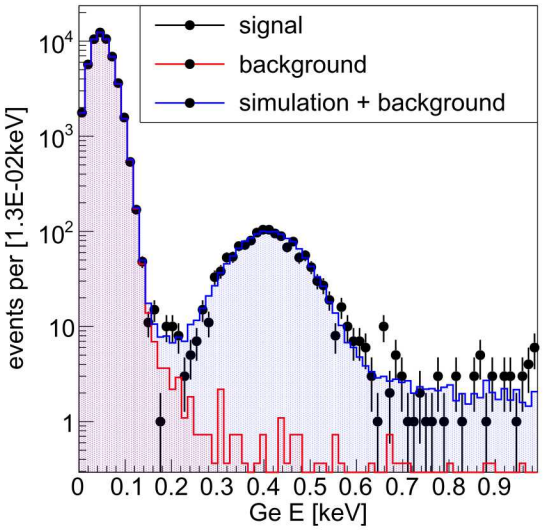

Figure 5.5. Comparison of the experimental signal spectrum with the *expectation* spectrum obtained with the parameters Θ^{max} as the sum of the the simulated spectrum and the normalized experimental background data.

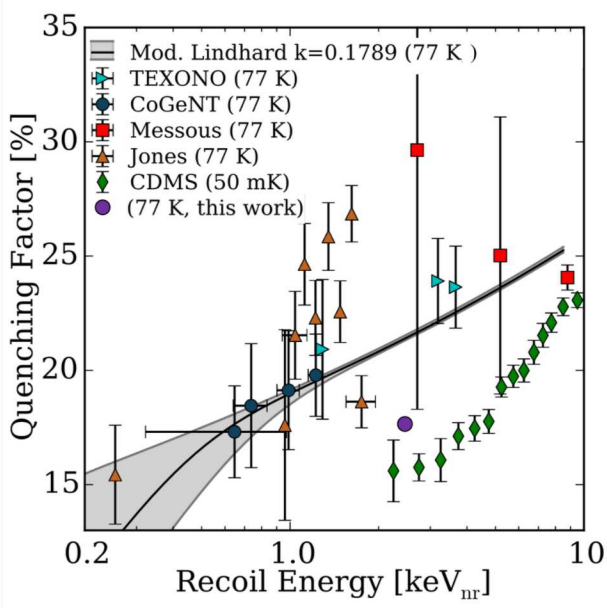

Figure 5.6. Our one result point $(Q, E_{\mathrm{nr}}) = (17.7\%, 2.317\ \mathrm{keVnr})$ compared to previous measurements. This plot has been extracted from [17].

potential cause for the σ_x smearing according to its dependance on frame distance and neutron beam energy.

Chapter 6

Conclusions

The data collected during the course of this project will allow the determination of the germanium quenching factor as a function of 10 discrete recoil energy values in the range $\sim [0.8, 5.0]$ keVnr. We have completed the simulation and data processing of 10 datasets, and have computed the quenching factor for one of them. Our one result seems to indicate a somewhat large deviation from literature values, though it is still preliminary to claim the presence of a systematic bias in our data or analysis. Fortunately, the two independent SNL and Duke analysis pipelines will provide a check on on each other results. Four more datasets, corresponding to lower recoil energies (as low as ~ 0.3 keVnr), were collected by our Duke collaborators. The analysis of those data will require a more careful analysis in order to extract the recoil signals that almost completely overlap with the noise pedestal.

References

[1] [Online]. Available: http://www.eljentechnology.com.

[2] [Online]. Available: http://www.struck.de/sis3316.html.

[3] C. E. Aalseth, P. S. Barbeau, J. Colaresi, J. I. Collar, J. Diaz Leon, J. E. Fast, N. E. Fields, T. W. Hossbach, A. Knecht, M. S. Kos, M. G. Marino, H. S. Miley, M. L. Miller, J. L. Orrell, and K. M. Yocum. Cogent: A search for low-mass dark matter using p-type point contact germanium detectors. *Phys. Rev. D*, 88:012002, Jul 2013.

[4] S. Agostinelli et al. Geant4: A simulation toolkit. *Nucl. Instrum. Methods in Phys Res.*, A506:250–303, 2003.

[5] D. Akimov, J. B. Albert, P. An, C. Awe, P. S. Barbeau, B. Becker, V. Belov, A. Brown, A. Bolozdynya, B. Cabrera-Palmer, M. Cervantes, J. I. Collar, R. J. Cooper, R. L. Cooper, C. Cuesta, D. J. Dean, J. A. Detwiler, A. Eberhardt, Y. Efremenko, S. R. Elliott, E. M. Erkela, L. Fabris, M. Febbraro, N. E. Fields, W. Fox, Z. Fu, A. Galindo-Uribarri, M. P. Green, M. Hai, M. R. Heath, S. Hedges, D. Hornback, T. W. Hossbach, E. B. Iverson, L. J. Kaufman, S. Ki, S. R. Klein, A. Khromov, A. Konovalov, M. Kremer, A. Kumpan, C. Leadbetter, L. Li, W. Lu, K. Mann, D. M. Markoff, K. Miller, H. Moreno, P. E. Mueller, J. Newby, J. L. Orrell, C. T. Overman, D. S. Parno, S. Penttila, G. Perumpilly, H. Ray, J. Raybern, D. Reyna, G. C. Rich, D. Rimal, D. Rudik, K. Scholberg, B. J. Scholz, G. Sinev, W. M. Snow, V. Sosnovtsev, A. Shakirov, S. Suchyta, B. Suh, R. Tayloe, R. T. Thornton, I. Tolstukhin, J. Vanderwerp, R. L. Varner, C. J. Virtue, Z. Wan, J. Yoo, C.-H. Yu, A. Zawada, J. Zettlemoyer, and A. M. Zderic. Observation of coherent elastic neutrino-nucleus scattering. *Science*, 2017.

[6] P S Barbeau, J I Collar, and O Tench. Large-mass ultralow noise germanium detectors: performance and applications in neutrino and astroparticle physics. *Journal of Cosmology and Astroparticle Physics*, 2007(09):009, 2007.

[7] A. Enqvist, C. C. Lawrence, B. M. Wieger, S. A. Pozzi, and T. N. Massey. Neutron light output response and resolution functions in ej-309 liquid scintillator detectors. *Nucl. Instrum. Methods in Phys Res.*, A715:79–86, 2013.

[8] D. Foreman-Mackey, D.W. Hogg, D.Lang, and J.Goodman. emcee: The mcmc hammer.

[9] J. Goodman and J. Weare. Ensemble samplers with affine invariance. *Comm. Appl. Math. and Comp. Sci.*, 5:65, 2010.

[10] K. W. Jones and H. W. Kraner. Energy lost to ionization by 254-ev ^{73}Ge atoms stopping in ge. *Phys. Rev. A*, 11:1347–1353, Apr 1975.

[11] A. C. Kaplan, M. Flaska, A. Enqvist, J. L. Dolan, and S. A. Pozzi. Ej-309 pulse shape discrimination performance with a high gamma-ray-to-neutron ratio and low threshold. A729:463–468, 2013.

[12] Glenn F Knoll. *Radiation detection and measurement; 4th ed.* Wiley, New York, NY, 2010.

[13] J. Lindhard, V. Nielsen, M. Scharff, and P.V. Thomsen. Integral equations governing radiation effects. *Mat. Fys. Medd.*, 33, 1963.

[14] Y. Messous. Calibration of a Ge crystal with nuclear recoils for the development of a dark matter detector. *Astropart. Phys.*, 3:361–366, 1995.

[15] M. A. Norsworthy, A. Poitrasson-Rivière, M. L. Ruch, S. D. Clarke, and S. A. Pozzi. Evaluation of neutron light output response functions in ej-309 organic scintillators. *Nucl. Instrum. Methods in Phys Res.*, A842:20–27, 2017.

[16] X. Ruan. Available from: http://wwwgerda.mpp.mpg.de/, 2011.

[17] B. J. Scholz, A. E. Chavarria, J. I. Collar, P. Privitera, and A. E. Robinson. Measurement of the low-energy quenching factor in germanium using an ^{88}Y/Be photoneutron source. *Phys. Rev. D*, 94:122003, Dec 2016.

[18] B. J. Scholz, A. E. Chavarria, J. I. Collar, P. Privitera, and A. E. Robinson. Measurement of the low-energy quenching factor in germanium using an ^{88}Y/Be photoneutron source. *Phys. Rev. D*, 94:122003, Dec 2016.

DISTRIBUTION:

1	MS 9406	Belkis Cabrera-Palmer, 8746
1	MS 9406	Kristin Hertz, 8746
1	MS 0899	Technical Library, 9536 (electronic copy)


Sandia National Laboratories